Fast assembly and *in vivo* coalescence of $ParB_F$ biocondensates involved in bacterial DNA partition

Perrine Revoil[1], Linda Delimi[2], Jérôme Rech[1], Josh Cailhau[2], François Cornet[1], Jean-Charles Walter[2]* and Jean-Yves Bouet[1]*

[1] Laboratoire de Microbiologie et Génétique Moléculaires, Centre de Biologie Intégrative (CBI), Centre National de la Recherche Scientifique (CNRS), Université de Toulouse, F-31062 Toulouse, France.

[2] Laboratoire Charles Coulomb (L2C), CNRS, Université de Montpellier, Montpellier, France.

*Correspondence should be addressed to jean-yves.bouet@univ-tlse3.fr and jean-charles.walter@umontpellier.fr

Classification: Biological science

Keywords: ParABS system, Partition complex, ParB, DNA segregation, Biomolecular condensates, Condensate coalescence.

Abstract

Faithful DNA segregation in bacteria relies on ParABS systems, in which ParB assembles into condensates at centromere-like *parS* sites and ParA, an ATPase, spatially organizes these complexes. Yet how ParB condensates preserve their dynamic behavior without collapsing into a single droplet has remained unclear. Here, we combined inducible chromosome degradation with quantitative imaging to dissect the kinetics and physical principles governing ParB condensate dynamics *in vivo*. In the absence of the nucleoid, ParB condensates from the plasmid F diffuse freely and coalesce within seconds upon encounter, following Brownian first-encounter statistics. Strikingly, condensates operate near the fusion-separation boundary, such that minimal energy is sufficient to split droplets after replication, thereby preventing irreversible coalescence. Using mutants, we demonstrate that condensate assembly is required for coalescence and uncover a dual role of $ParA_F$: while nucleoid tethering limits condensate mobility and prevents uncontrolled fusion, $ParA_F$ also promotes a $ParB_F$ state competent for condensate assembly and coalescence, likely by enhancing $ParB_F$-$ParB_F$ interactions. Finally, condensates rapidly disassemble and reassemble upon 1,6-hexanediol treatment, underscoring their reversible, dynamic nature and the stabilizing contribution of ParB-DNA interactions. Together, our results establish $ParB_F$ partition complexes as *bona fide* biocondensates and reveal how their dynamics are finely tuned by $ParA_F$ to ensure robust and faithful DNA segregation. More broadly, these findings highlight regulated phase separation as a key organizing principle of bacterial replicons.

Significance statement

Faithful chromosome and plasmid segregation is essential for bacterial survival, yet the underlying physical principles remain unclear. We show that ParB partition complexes are *bona fide* biomolecular condensates whose fusion-fission dynamics are tightly regulated to prevent collapse into a single droplet. Using quantitative imaging with inducible chromosome degradation, we demonstrate that ParB condensates operate near the fusion-separation boundary, where minimal energy allows splitting. We uncover a dual role of the ATPase ParA: tethering condensates to the nucleoid and promoting their assembly. These findings further establish ParB condensates as phase-separated nucleoprotein complexes and reveal how their dynamics are tuned to ensure robust DNA segregation, underscoring phase separation as a key principle of bacterial cell organization.

Introduction

Bio-molecular condensates, also referred as membrane-less organelles, are key organizational units in living systems, facilitating a wide range of cellular processes (Alberti et al., 2025; Boeynaems et al., 2018). They have been widely reported in eukaryotes, and more recently in bacteria where they concentrate proteins and nucleic acids without the need for a lipid membrane (Azaldegui et al., 2021; Cohan and Pappu, 2020). In bacteria, such condensates contribute to diverse processes, including transcription (Ladouceur et al., 2020), mRNA decay (Al-Husini et al., 2018), and the partitioning of intracellular cargos, such as carboxysomes in autotrophic bacteria (Basalla et al., 2023; MacCready et al., 2020) and DNA centromeres from plasmids and chromosomes (Babl et al., 2022; Guilhas et al., 2020; Zhao et al., 2024).

Active DNA partitioning in bacteria is primarily driven by the ParABS system, widely found on low-copy-number plasmids and the only one present on chromosomes (Bouet and Funnell, 2019). This system is composed of three components: two proteins, ParA and ParB, and a centromeric sequence, *parS*. Together, these elements are necessary and sufficient to ensure accurate plasmid inheritance. ParB assembles into higher-order nucleoprotein complexes at *parS* sites, while ParA, an ATPase, spatially localizes these partition complexes through dynamic interaction with the nucleoid. In its ATP-bound form, ParA associates with DNA and interacts with the cargo via ParB, which stimulates its ATPase activity and promotes its release from DNA (Ah-Seng et al., 2013; Azaldegui et al., 2026; Lim et al., 2014; MacCready et al., 2018; Vecchiarelli et al., 2010). This interaction generates local ParA depletion zones on the nucleoid, driving directional cargo movement toward regions of higher ParA concentration (Hu et al., 2021; Hu et al., 2015; Hwang et al., 2013; Walter et al., 2017). In the plasmid F system, a subset of $ParA_F$ also associates with high-density-regions of the nucleoid and contributes to anchoring $ParB_F$ condensates within the nucleoid (Hu et al., 2021; Le Gall et al., 2016). Following DNA replication and duplication of ParB-*parS* complexes, ParA mediates their separation and relocation to opposite cell halves, ensuring faithful inheritance upon cell division (Bouet and Funnell, 2019; Jalal and Le, 2020).

Partition complexes regroup over 80% of ParB at centromere sites (Lim et al., 2014; Sanchez et al., 2015). Their assembly are initiated by a sequential multi-step process: (i) specific binding of ParB to *parS*, typically a 16-bp DNA motif (Lin and Grossman, 1998; Livny et al., 2007; Pillet et al., 2011), (ii) CTP binding to *parS*-bound ParB (Jalal et al., 2020; Osorio-Valeriano et al., 2019; Soh et al., 2019), (iii) conversion of ParB into a sliding clamp, promoting its release from *parS* (Jalal et al., 2021; Osorio-Valeriano et al., 2021; Soh et al., 2019), (iv) diffusion at short distances along *parS*-proximal DNA (Alaoui et al., 2025; Soh et

al., 2019), and (v) clamp opening followed by ParB unloading (Antar et al., 2021; Jalal et al., 2020). ParB thus cycles between open and clamped forms, called the ParB-CTP cycle, enabling the loading of ParB clamps specifically at *parS* sites. Notably, both chromosomal and plasmid ParABS systems form partition complexes that display hallmarks of biomolecular condensates (Babl et al., 2022; Guilhas et al., 2020), characterized by a high-density ParB phase coexisting with a dilute phase, likely arising from phase separation (Azaldegui et al., 2021; Monterroso et al., 2024). This behavior has been proposed to rely on a CTP-dependent molecular switch that enhances interactions between ParB dimers (Delimi et al., 2025; Tisma et al., 2024; Tisma et al., 2022), thereby driving strong local enrichment of ParB (Balaguer et al., 2021; Guilhas et al., 2020; Sanchez et al., 2015; Zhao et al., 2024). In addition, ParB clamp-mediated bridging between distant DNA segments may further stabilize these assemblies (Balaguer et al., 2021; Connolley et al., 2023; Taylor et al., 2021; Tisma et al., 2023; Zhao et al., 2024), forming the higher-order nucleoprotein complexes that dynamically interact with ParA to ensure the segregation of chromosomal origins and plasmids (Jalal and Le, 2020).

Biomolecular condensates typically exhibit liquid-like properties, including spherical shapes, rapid exchange of components between condensed and diffuse phases, and coalescence into larger droplets (Shin and Brangwynne, 2017). Partition complexes in the plasmid F system displays these features *in vivo*, including rapid exchange of $ParB_F$ between complexes (Debaugny et al., 2018), reduced intracellular mobility of $ParB_F$ within rounded condensates (~100-fold lower than outside) (Guilhas et al., 2020), and fusion events upon $ParA_F$ depletion (Guilhas et al., 2020). At thermodynamic equilibrium, in a finite and confined system, phase separation with a condensed phase minimizes interfacial free energy by forming a single condensate, with coalescence or Ostwald ripening driving this process (Hyman et al., 2014). However, in ParABS systems, this intrinsic tendency toward coalescence conflicts with the functional requirement to maintain multiple, spatially separated ParB condensates to ensure faithful DNA partition. Although $ParA_F$ depletion induces condensate fusion (Guilhas et al., 2020), these events occur slowly, likely due to sustained high expression of $ParA_F$ prior to its gradual degradation, limiting quantitative analysis of coalescence dynamics.

Here, we developed an inducible chromosome degradation system to probe the behavior of ParB condensates in the absence of the nucleoid. Under these conditions, $ParB_F$ condensates diffuse freely and coalesce within seconds upon encounter, enabling direct measurement of coalescence kinetics. We further show that condensate assembly is rapid, reversible, and

dependent on hydrophobic interactions, as revealed by hexanediol sensitivity. Importantly, our results uncover a previously unappreciated function of $ParA_F$, beyond nucleoid tethering, in promoting $ParB_F$ condensate assembly. Together, these functions regulate the fusion-fission balance of $ParB_F$ condensates, maintaining their dynamic stability and ensuring robust and faithful segregation of bacterial DNA.

Results

Chromosome depletion triggers coalescence of ParB condensates

$ParB_F$ condensates are typically anchored within the nucleoid via interactions with $ParA_F$, which binds to the high-density regions of DNA (Le Gall et al., 2016). To investigate the dynamics and conditions that promote fusion of $ParB_F$ condensates, we developed a strategy to disrupt this anchoring by selectively removing the bacterial chromosome. We hypothesized that depleting the nucleoid would free $ParB_F$ condensates to diffuse throughout the cytoplasm, facilitating their coalescence, if any. To test this, we employed a method for specific and progressive chromosome degradation while preserving plasmid integrity (Stracy et al., 2021). We constructed an *E. coli recA* strain (DLT4151) carrying four I-SceI restriction sites evenly distributed across the chromosome (Fig. 1A). This strain was transformed with pSN01, which expresses the I-SceI endonuclease under the control of arabinose, enabling inducible double-strand breaks and subsequent chromosome degradation. The amount of nucleoid per cell was monitored over time using DAPI staining and fluorescence microscopy (Fig. 1B, left panels). Upon arabinose-induced I-SceI production, DAPI fluorescence intensity gradually decreased to near-baseline levels over ~100 minutes, confirming progressive loss of chromosomal DNA (Supplementary Fig. S1A-C). By 120 minutes post-induction (T120), chromosomal DNA was extensively degraded in nearly all cells.

We then examined the behavior of $ParB_F$ condensates in the absence of the nucleoid. F plasmids producing $ParB_F$-mVenus fusion proteins were introduced in the DLT4151 strain, which was further transformed with pSN01. In steady-state growth, prior to induction (T0), cells carrying the 100-kbp F plasmid (F1-10B04) typically exhibited two $ParB_F$-mVenus foci. After chromosome degradation (T120), 88.4% of cells contained only a single focus (Fig. 1B, right panel and Fig. 1C, left panel). To directly observe these fusion events, we performed time-lapse imaging at 2-minute intervals. Fusion was defined as the merging of two foci that subsequently moved together during several successive images (Fig. 1D). Most fusion events occurred between 70 to 90 minutes post-induction, corresponding to ~75-90 % of chromosome degradation (dotted line). By T120, when chromosome degradation was

completed, fusion events had occurred in 95% of the cells, as shown by the cumulative curve (black line).

To assess whether plasmid size affects condensates fusion, we repeated the experiment using a ~10-kbp mini-F plasmid (pJYB234). Similar coalescence kinetics were observed, with over 90 % of the cells exhibiting fusion events, as with the 100-kbp plasmid (Fig. 1C, central panel and Supplementary Fig. S1D). This finding indicate that condensate fusion is independent of plasmid size.

To ensure that plasmids do not spontaneously cluster in the absence of the chromosome, we monitored the behavior of a mini-F lacking the *par* system, labelled with a FROS system allowing us to track plasmids devoid of partition complexes (Fig. 1C, right panel). Due to defective partitioning, this Δ*par* mini-F (pPER07) was frequently lost, resulting in a high proportion of plasmid-free cells, *i.e.* cells without foci (62%). Among cells retaining the plasmid, the proportions with one (17.3%) or two (16.9%) foci remained unchanged before (T0) and after complete chromosome degradation (T120). These results demonstrate that, in nucleoid-free cells, low-copy-number plasmids do not cluster together in the absence of the ParABS system.

Defects in ParB multimerization impair condensate fusion

To determine whether the fusion events observed in nucleoid-free cells reflect an intrinsic property of $ParB_F$ condensates, we analyzed a ParB variant, $ParB_F$-R156A, previously shown to partially impair condensate formation and partition activity (Delimi et al., 2025). This mutation, located in the box III motif involved in CTP binding and hydrolysis (Osorio-Valeriano et al., 2021) still allows $ParB_F$-R156A to bind to $parS_F$ and form clamps but disrupts ParB-ParB interactions necessary for higher-order assembly (Delimi et al., 2025). We monitored cells carrying an F plasmid expressing $ParB_F$-R156A-mVenus before (T0) and after I-SceI induction (Fig. 2A, top panel). At T0, 15% of the cells lacked detectable foci, consistent with plasmid loss due to defective partitioning (Fig. 2A, bottom panel), compared to 1.5 % in the wild-type (Fig. 1C). At T120, a shift from two foci to one was observed, indicating that coalescence can occur. However, this effect remained limited: the proportion of one-focus cells increased by ~18%, and two-focus cells decreased by ~19%, in contrast to 58% and 47%, respectively, for the WT. Moreover, at T120, only 50 % of chromosome-depleted cells exhibited fusion events, and with delayed kinetics (Fig. S1E), compared to ~95% in wild-type (Fig. 1D). These results indicate that partial defect in $ParB_F$ condensate assembly substantially reduces the frequency and efficiency of their fusion.

Consistent with this defect, $ParB_F$-R156A-mVenus displayed a markedly diffuse fluorescence pattern with less-defined condensates compared to the $ParB_F$-mVenus (Fig. 2A versus Fig. 1B). To quantify this difference, we performed a skewness analysis of fluorescence intensity distributions, which reports on the asymmetry of intracellular signal. Higher skewness values correspond to a few bright pixels for a majority of low intensity pixels, or punctate foci (*i.e.*, well-formed condensates), whereas close to zero values indicate diffuse fluorescence. This metric thus provides a quantitative proxy for ParB condensates assembly (Fig. 2C). In WT plasmid, $ParB_F$-mVenus formed bright foci with an average skewness of 1.85 (N=144). In contrast, cells carrying a mini-F Δ*parS* plasmid, which cannot nucleate ParB condensates, displayed near-baseline skewness (0.19; N=411). The $parB_F$-R156A condition showed intermediate skewness values (0.70; N=269), indicating defective condensate assembly. These results support the conclusion that impaired ParB self-association compromises both condensate formation and their ability to undergo fusion.

$ParA_F$ has an effect on the coalescence of $ParB_F$ condensates

$ParA_F$ plays a central role in positioning partition complexes along the nucleoid (Hu et al., 2021; Le Gall et al., 2016). In its ATP-bound form, $ParA_F$ interacts with both $ParB_F$ and non-specific DNA (nsDNA) (Bouet et al., 2007; Castaing et al., 2008), and has been proposed to promote $ParB_F$-$ParB_F$ interactions (Taylor et al., 2021). To test whether $ParA_F$ also contributes to condensate coalescence, we analyzed a plasmid F Δ$parA_F$ (F1-10B12), expressing $ParB_F$-mVenus from an inducible P*tet* promoter. Western blot analysis indicated that $ParB_F$-mVenus levels were about two-fold lower than in the wild-type, where expression is driven by the native $ParA_F$ auto-regulated promoter (Fig. S2). Despite this reduction, partition condensates were readily detectable (Fig. 2B, top). We quantified the number of ParB foci per cell before (T0) and after (T120) I-SceI induction (Fig. 2B, bottom). At T0, 43% of the cells lacked foci, consistent with defective partitioning in the absence of $ParA_F$ (Le Gall et al., 2016). Following chromosome degradation (T120), only a modest shift was observed: the proportion of one-focus cells increased by 7%, while two-focus cells decreased by 6.4%. This contrasts sharply with the wild-type condition (Fig. 1D), indicating that the absence of $ParA_F$ strongly impairs coalescence of ParB condensates in the absence of chromosome.

ParB fluorescence in cells carrying a Δ$parA_F$ plasmid appeared more diffuse (Fig. 2B), similar to that observed for the $ParB_F$-R156A variant (Fig. 2A). Skewness analysis yielded an intermediate value (0.72; N=152) (Fig. 2C), comparable to that obtained with $ParB_F$-R156A.

This partial defect likely reflects impaired $ParB_F$-$ParB_F$ interactions upon loading at $parS_F$, preventing efficient condensation of the majority of $ParB_F$.

Together, analyses of the $parB_F$-R156A mutant and the $\Delta parA_F$ condition demonstrate that, in the absence of the nucleoid, condensate coalescence is severely impaired when ParB self-association is disrupted. In both cases, reduced fusion correlates with defective condensate assembly, indicating that efficient coalescence requires a properly assembled condensate state. We therefore conclude that $ParA_F$, in addition to its role in spatial organization, promotes ParB condensate assembly, thereby enabling their fusion in the absence of chromosome.

Coalescence into a single condensate is a conservative process

Condensates naturally tend to fuse into fewer, larger assemblies, as droplet coalescence minimizes surface tension and free energy, thereby reaching a more thermodynamically stable state (Hyman et al., 2014). However, the diffraction limit of fluorescence microscopy prevented us from directly measuring the size of individual ParB condensates before and after fusion. To overcome this technical limitation, we used fluorescence intensity as a proxy for condensate size. This approach relies on our previous finding that the ParB concentration inside condensates is comparable to the overall protein concentration in the cytoplasm, suggesting that condensates accumulate ParB up to a cytoplasmic saturation threshold (Guilhas et al., 2020). Under these conditions, fluorescence intensity is thus expected to scale with condensate volume.

We measured the fluorescence intensity of ParB-mVenus foci in 50 cells, before and after fusion events. On average, the post-fusion intensity was 0.94 times the sum of the two pre-fusion foci (Fig. 3A and Fig. S3). This indicates that the majority of ParB molecules are retained within the resulting condensate, consistent with a conservative coalescence process in which little to no ParB is lost or dispersed. This finding supports the idea that fusion results in the formation of larger condensates.

We next asked whether more than two foci can coalesce into a single one. To test this, we treated cells with cephalexin, a β-lactam antibiotic that blocks cell division without inhibiting DNA replication. This treatment led to cell elongation and increased the plasmid copy number per cell. After one hour of cephalexin treatment, cells approximately doubled in size, and ParB foci ranged from 1 to 8, with an average of 4.2 foci per cell (Fig. 3B). Following chromosome degradation, 88% of cells displayed a single ParB focus at T120, indicating that most ParB condensates had fused into a single one.

These findings support the view that ParB condensates behave as droplets undergoing coalescence. Regardless of plasmid copy number, ParB condensates reliably fuse into fewer, larger assemblies to minimize surface tension. This process is largely conservative, retaining all ParB molecules within the fused condensates.

ParB-DNA condensates operate near the fusion-separation boundary

Our measurements showed that 95 % of chromosome-depleted cells had undergone partition condensates fusion within 120 min of chromosome degradation induction (Fig. 1E). We were curious about the remaining ~5% of cells in which fusion was not observed at T120. Closer inspection revealed that some cells displaying a single fused focus at earlier time points latter exhibited splitting events. To explore this phenomenon, we performed high-frequency imaging, acquiring frames every 250 milliseconds over 30-second (Fig. 4A). Despite this brief time window, we detected splitting events in ~10 % of cells carrying the plasmid F (Fig. 4B), suggesting that splitting is a frequent event, potentially occurring approximately once every five minutes per cell on average. When examining cells carrying the smaller mini-F, splitting events were detected in 18% of cells, indicating that condensates derived from smaller plasmids split more frequently than those from larger plasmids. This suggests that, in the absence of chromosome, a smaller DNA amount near *parS* sites permits more frequent escape of one plasmid from condensates. Moreover, the frequency of splitting events was slightly higher in Δ*parA* derivatives (Fig. 4B), suggesting that fused condensates formed either from smaller DNA molecules or in the absence of ParA are more prone to dissociation. In all cases, however, splitting events were transient, as the separated foci consistently fused back after a short period of time (Fig. 4A).

In nucleoid-depleted cells, condensates are fused ~90% of the time but still undergo occasional splitting, suggesting that the system operates near a crossover regime between fused and separated states, with a free energy difference approaching zero, *i.e.*, within the fused region of the phase diagram but close to the transition line ($\Delta F \sim 0$). To quantitatively understand this equilibrium, we developed a coarse-grained polymer model that captures the competition between surface energy minimization and configurational entropy loss during condensate coalescence (see Supplementary Methods). At the fusion-separation transition, we estimated a critical surface tension γ_{crit} = 0.80 +/- 0.21 $\mu N.m^{-1}$ for the F plasmid (N = 660; Figure S6). Given that ParABS systems are naturally found on replicons spanning a wide range of size, from ~25 kbp to over 1 Mb (Planchenault et al., 2020), we extend our analysis

and calculated a γ_{crit} = 1.10 +/- 0.29 µN.m^{-1} for a 1 Mb DNA molecule. For the smaller mini-F used in this study (pJYB234, ~10 kbp; N = 60), we measured a γ_{crit} = 0.49 +/- 0.13 µN.m^{-1} (Figure S6). These values place the tension surface of ParB-DNA droplets, across a large range of DNA size replicons, within the typical 0.1-1 µN.m^{-1} range observed in biological phase-separated systems (Holland et al., 2023). This supports the conclusion that ParB-DNA condensates operate near the fusion-separation boundary, with entropy costs remaining negligible over biologically relevant DNA lengths.

Coalescence of partition condensates occurs rapidly

The dynamic splitting-fusion behavior observed for ParB foci provided an opportunity to investigate the kinetics of condensate coalescence. Using the frame where a splitting event was first observed as time zero, we measured the time required for ParB condensates to fuse back together. Analysis of 111 such events from the F plasmid revealed that re-fusions occurred, on average, within approximately one second (Fig. 4C). This result demonstrates that coalescence of partition condensates is a rapid process, nearly instantaneous compared to the time of splitting, the cell cycle or to DNA replication. To further characterize the fusion kinetics, we plotted the number of fusion events over time on a log-log scale and found that the distribution fit well to a power law with an exponent of -3/2 (Fig. 4C, inset). This scaling suggests that the coalescence times are consistent with a first encounter of two Brownian particles (Byczkowski et al., 2013). Such behavior is consistent with free diffusion of condensates in the absence of chromosome, where condensate collisions and subsequent fusions are governed by random Brownian motion.

To assess the mobility of partition condensates, we compared their diffusive behavior in the presence and absence of the chromosome. $ParB_F$-mVenus foci from both plasmid F and mini-F were tracked using high-resolution time-lapse microscopy, with images acquired every 0.5 second over a 30 seconds period. In chromosome-depleted cells, condensates exhibited markedly enhanced mobility (Fig. S4): the mean step size (*Ss*) between frames increased by 6-fold for mini-F (*Ss* ~ 1.8 µm) and 4-fold for plasmid F (*Ss* ~ 1.2 µm) compared to cells with intact chromosomes (*Ss* ~ 0.3 µm). We quantified this difference by computing the mean square displacement (MSD) of $ParB_F$ foci to estimate diffusion coefficients (D) under both conditions (Fig. 4D and Fig. S4), using a sub diffusive model:

$$MSD(t) = D_{\alpha} \, . \, t^{\alpha}$$

where D_α is the generalized diffusion coefficient (μm² $s^{-\alpha}$) and α is the scaling exponent describing the nature of particle motion (see Eq. (5) in Supplemental methods). In the presence of the chromosome, α values of 0.81 (F) and 0.88 (mini-F) reflected sub-diffusive, constrained dynamics (Parry et al., 2014). Upon chromosome removal, α rose to 0.92 and 0.95, respectively, approaching the theoretical value for Brownian (free) diffusion (α = 1). The corresponding D_α values increased by 10-40 fold, from 0.001-0.002 μm² $s^{-\alpha}$ to 0.04 and ~0.02 μm² $s^{-\alpha}$. Notably, the rise in D_α scales approximately with the square of the step size, confirming that the exponents α are sufficiently close to 1 to approximate D_α to an usual diffusion coefficient at short time scales. Together, these results show that $ParB_F$ condensates behave as nearly freely diffusing particles in the absence of chromosome, and suggest that their mobility is primarily limited by condensate size rather than the length of the plasmid DNA carrying $parS_F$.

Partition condensates assemble and disassemble within seconds

In biological phase separation, biomolecular interactions, such as protein-protein and protein-nucleic acid interactions, underpin the formation and stability of condensates. The ParB condensates formed on plasmid F enables the dissection of the individual roles of these two interactions within cells almost completely depleted of non-specific DNA. To test the role of weak intermolecular interactions in condensate stability, we used 1,6-hexanediol (Hex), an aliphatic alcohol that interferes with hydrophobic interactions (Kroschwald, 2017).

Cells expressing $ParB_F$-mTq2 from mini-F along with a FROS reporter MalI-mNG[2] (bound to 7 *malO* sites present on the plasmid, pPER08) were deprived from their chromosome and, when ~95% of cells displayed fused partition condensates (T120), were treated with 10 % Hex. After one minute, ParB-mTq2 fluorescence became diffuse in most cells (89.3%), indicating efficient condensates dissolution (Fig. 5A and Fig. S5). In contrast, MalI-mNG2 foci remained intact, showing that specific protein-DNA interactions were preserved. Interestingly, some cells displayed two MalI foci following Hex treatment, suggesting that plasmids, previously held together within the same condensate, were now free to diffuse apart, further supporting that coalescence is mediated by weak and/or non-specific interactions (Fig. S5A).

To investigate the kinetics of $ParB_F$ condensate disassembly, we performed time-lapse imaging during Hex infusion (Fig. 5B, top left). $ParB_F$ fluorescence became visibly diffuse as early as 7 seconds after treatment and foci disappeared almost completely by 47 seconds. To

quantify the Hex-induced disassembly, we measured the fluorescence skewness across 1150 cells (Fig. 5B, right). Before Hex addition, skewness was ~2.11, slightly higher than measured in the presence of nucleoid (1.85; Fig. 2C). Upon Hex treatment, the average skewness progressively decreased to ~0.84 and 0.47 after 7 and 27 seconds, respectively, reaching a plateau at ~0.33 by 47 seconds. This plateau value is slightly above the skewness observed when all $ParB_F$ are diffusive (0.19; Fig. 2C), consistent with only a small fraction of $ParB_F$ remaining bound to $parS_F$ or clamped nearby.

We then tested whether $ParB_F$ condensates could reassemble after washing out Hex. Following a 100-seconds Hex exposure, cells were infused in buffer without Hex (Fig. 5B, bottom left). Within 7 seconds, skewness rapidly increased to 1.49, and by 27 seconds, it reached a value above 2, restoring the pre-treatment level and showing complete $ParB_F$ condensates reassembly (Fig. 5B, right). Strikingly, the kinetics of reassembly mirrored that of disassembly, both occurring within seconds.

Altogether, these data demonstrate that $ParB_F$ condensates disassemble and reassemble rapidly and reversibly in response to disruption and restoration of weak hydrophobic interactions, respectively. In the absence of the nucleoid, this behavior strongly suggests that the internal cohesion of partition condensates is primarily driven by reversible $ParB_F$-$ParB_F$ interactions.

Partition condensates assembly requires both $ParB_F$-$ParB_F$ and $ParB_F$-DNA interactions

To assess the relative contributions of $ParB_F$-$ParB_F$ and $ParB_F$-nsDNA interactions to condensate assembly, we repeated hexanediol treatment experiments in cells with intact nucleoids (Fig. 5C). Under these conditions, condensate disassembly occurred slightly more slowly than in nucleoid-depleted cells, with skewness reaching a plateau within 47 seconds. Following Hex washout, $ParB_F$ condensates reassembled almost completely within 7 seconds, indicating that the disruption and restoration of $ParB_F$-$ParB_F$ interactions proceed with slightly slower and faster kinetic, respectively, compared to nucleoid-depleted cells. Notably, while disassembly was nearly complete in nucleoid-depleted cells (plateau skewness ~0.33), it was only partial in the presence of the chromosome, with skewness stabilizing at ~1.2. These results indicate that, in addition to $ParB_F$-$ParB_F$ interactions, $ParB_F$-DNA interactions substantially contribute to condensate integrity and assembly kinetics.

To further probe these interactions, we performed the hexanediol treatment in cells carrying a plasmid F encoding the $ParB_F$-R156A variant (F1-10B15), which exhibits impaired $ParB_F$-$ParB_F$ interactions and reduced condensate formation (Fig. 2A, C). In nucleoid-

depleted cells, $ParB_F$-R156A-mVenus skewness dropped rapidly from 1.04 to 0.29 within 7 seconds, reaching a plateau at ~0.21 (Fig. S5B). This value closely matched that of fully diffuse $ParB_F$ in the absence of condensates (~0.19; Fig. 2C), indicating near-complete dissolution. In the presence of the nucleoid, skewness decreased from 0.81 to 0.36, plateauing at ~0.28 (Fig. S5C), slightly higher than in the nucleoid-free conditions but still indicative of near-total condensate disassembly.

Notably, in both WT and $ParB_F$-R156A backgrounds, condensate disassembly was slower and less complete in the presence of the nucleoid than in its absence (Fig. 5B, C and Fig. S5B, C). Conversely, condensate reassembly after hexanediol washout occurred slightly rapidly when the nucleoid was present. These kinetic differences underscore the contribution of $ParB_F$-nucleoid interactions both in buffering condensates against chemical-induced disruption and in facilitating their rapid reformation.

A side-by-side comparison of WT and $ParB_F$-R156A condensates across all conditions using skewness quantification (Fig. 5D) further supports that (i) condensates form in both nucleoid-containing and -depleted cells (a-d), (ii) both hexanediol treatment and the $ParB_F$-R156A variant cause partial defects in condensate formation (compare c and e to a), indicating that $ParB_F$-$ParB_F$ interactions are necessary but not sufficient for robust condensate assembly, and (iii) simultaneous nucleoid removal and perturbation of $ParB_F$-$ParB_F$ interactions (f) results in complete condensate disassembly.

Together, these findings establish that $ParB_F$ condensate assembly is a cooperative process driven by both $ParB_F$-$ParB_F$ and $ParB_F$-DNA interactions, with maximal cohesion and stability arising from their synergistic interplay.

Discussion

ParB condensates as a paradox of DNA segregation

In this study, we investigated the dynamics of $ParB_F$ condensates involved in bacterial DNA partition, uncovering key kinetic and mechanistic features that define their behavior *in vivo*. Faithful segregation of low-copy-number genetic elements requires at least two partition complexes to remain physically separated on either side of the septum before cell division. This requirements presents a fundamental paradox: biomolecular condensates formed by phase separation inherently tend to coalesce into a single droplet to minimize surface tension and free energy (Azaldegui et al., 2021). ParABS-mediated partition systems offer a powerful model for understanding how cells reconcile this conflict. Growing evidence indicates that ParB assemblies exhibit droplet-like properties both *in vivo* (Guilhas et al., 2020) and *in vitro*

(Babl et al., 2022), making them well-suited to address how phase-separated condensates can remain stable as multiple entities inside a single bacterial cell.

Chromosome removal reveals coalescence dynamics

Previous work showed that $ParB_F$ condensates eventually merge *in vivo* following $ParA_F$ depletion using a degron-based approach (Guilhas et al., 2020). However, fusion events became detectable only after overnight growth, due to continuous $ParA_F$ overproduction followed by its gradual degradation, thereby precluding accurate analysis of coalescence kinetics. In the absence of $ParA_F$, $ParB_F$ condensates largely remain separated, likely because (i) their physical exclusion from the nucleoid confines them to the cell poles (Le Gall et al., 2016), limiting their probability of encounter and, (ii) they exhibit a reduced propensity to coalesce, consistent with a role for $ParA_F$ in promoting $ParB_F$ condensates assembly (see below).

To overcome these limitations, we developed a chromosome degradation approach that eliminates $ParA_F$-dependent anchoring of ParB condensates to the nucleoid, thereby enabling their unrestricted diffusion in the cytoplasm. Under these conditions, nearly all $ParB_F$ condensates coalesce within 120 minutes of chromosome removal (Fig. 1B-D and Fig. S1), independently of their initial number (Fig. 3B). The resulting condensates exhibit high mobility, with diffusion coefficients reaching ~0.02 and ~0.04 $\mu m^2\ s^{-1}$ for F and mini-F plasmids, respectively, which is more than 10-fold higher than in nucleoid-containing cells (~0.002 and ~0.001 $\mu m^2\ s^{-1}$) (Fig. 4D and Fig. S4). These values are comparable to diffusion rates reported for large nucleoprotein assemblies in *E. coli*, such as polysomes (~0.04 $\mu m^2\ s^{-1}$), but remain lower than those of free ribosomal subunits (~0.2 $\mu m^2\ s^{-1}$) (Bakshi et al., 2012; Sanamrad et al., 2014). In nucleoid-free cells, the scaling exponent α derived from MSD analysis approaches ~ 1, indicative of near-free Brownian motion, whereas in the presence of the chromosome, sub-diffusive values ($\alpha < 0.9$) reflect constrained mobility. Together, these results strongly suggest that, in the absence of the nucleoid, the mobility of $ParB_F$ condensates is primarily governed by their physical size, rather than by the length of the $parS_F$-carrying plasmid.

Using transient splitting of $ParB_F$ condensates as a reference point, we measured fusion times of ~1 second (Fig. 4A-C). Such near-instantaneous coalescence upon contact indicates a droplet fusion process rather than Ostwald ripening (Hyman et al., 2014). Moreover, the power-law distribution of coalescence times is consistent with first-encounter kinetics between diffusing particles, underscoring the stochastic nature of condensate collisions.

Importantly, the increased mobility observed upon nucleoid removal directly enhances encounter rates, thereby promoting rapid coalescence. These findings indicate that nucleoid tethering, mediated by $ParA_F$, not only spatially organizes condensates but also kinetically limits their fusion by constraining their diffusion.

Strikingly, our analysis further indicates that $ParB_F$ condensates operate near the fusion-separation boundary (Fig. S6), implying that only minimal energy is required either to separate fused droplets or to split condensates generated by partition complex duplication during replication. Operating at this boundary is likely crucial for DNA segregation, as it prevents irreversible coalescence into a single droplet while maintaining sufficient plasticity for dynamic reorganization. This finely tuned fusion-fission balance highlights how condensate phase behavior is optimized *in vivo* and raises the possibility that $ParA_F$ may facilitate condensate separation with only a minimal energetic input. Alternatively, the initial separation step may occur independently of $ParA_F$, as proposed for ParA from *C. crescentus* (Puentes-Rodriguez et al., 2023; Shebelut et al., 2010), where SMC (Structural Maintenance of Chromosome) proteins contribute to the separation of the replicated origins (Lee and Grossman, 2006). In light of this finding, the role of ParAs in driving the separation of duplicated partition complexes or other condensates such as carboxysomes (Ah-Seng et al., 2013; Byrne et al., 2025) warrants further investigation.

ParA regulates both condensate positioning and assembly

Our results reveal that proper condensate assembly is essential for efficient coalescence. Perturbing the ability of $ParB_F$ to form condensates (Fig. 2C), while preserving its capacity to bind to $parS_F$ and diffuse nearby, strongly impaired coalescence, as observed with the $ParB_F$-R156A variant (Fig. 2A). A similar reduction in coalescence was also observed in the absence of $ParA_F$ (Fig. 2B). These observations suggest that $ParA_F$ contributes to the formation of a condensate-competent state of $ParB_F$ *in vivo*, most likely by stimulating $ParB_F$-$ParB_F$ interactions as observed *in vitro* (Taylor et al., 2021). Consistent with this view, ChIP-seq analyses have shown that ParB DNA-binding patterns are altered in the absence of ParA, suggesting impaired higher-order assembly (Donczew et al., 2016).

Our data therefore point to two complementary roles of $ParA_F$. First, $ParA_F$ promotes the efficient assembly of ParB condensates, enabling the cohesive interactions required for condensate fusion. Second, through its well-established role in tethering partition complexes to the nucleoid (Le Gall et al., 2016), $ParA_F$ spatially separates condensates and thereby limits

their encounters. In this framework, $ParA_F$ simultaneously enhances the intrinsic fusion competence of condensates while reducing the probability that such fusion events occur.

Consistent with this interpretation, splitting events became slightly more frequent in the absence of $ParA_F$, particularly for $ParB_F$ condensates assembled on large plasmids (Fig. 4B). This suggests that condensates formed without $ParA_F$ are less cohesively assembled and therefore more prone to separate after transient contacts, presumably due to weaker $ParB_F$-$ParB_F$ interactions. Thus, while the absence of $ParA_F$ relaxes spatial constraints that normally keep condensates apart, it simultaneously reduces their capacity to fuse by weakening condensate assembly. Altogether, these results identify $ParA_F$ as a dual regulator that coordinates the assembly and spatial organization of ParB condensates. By promoting condensate cohesion while maintaining their spatial separation within the nucleoid, $ParA_F$ ensures that partition complexes remain both properly assembled and correctly positioned for faithful segregation.

Rapid kinetics of ParB condensates assembly

ParB condensates associated with plasmids or chromosomes are continuously present in cells, provided that at least one cognate *parS* site is present (Bouet and Funnell, 2019). Disassembly and reassembly of the $ParB_F$ complex have been reported to occur within less than a minute during replication of the $parS_F$ centromere region (Walter et al., 2020). In chromosome-depleted cells treated with 1,6-hexanediol, which disrupts weak hydrophobic interactions (Kroschwald, 2017), we find that these kinetics are even faster, occurring within only a few seconds, with most $ParB_F$ dispersing over the nucleoid (Fig. 5A-B). This treatment, intended to disrupt interactions between ParB dimers, may also interfere with the *parS*- and CTP-dependent intra-dimer association of the two N-terminal domains of $ParB_F$ (Jalal et al., 2021; Soh et al., 2019), thereby promoting clamp opening and condensates disassembly. It may also perturb $ParA_F$-$ParB_F$ interactions which are shown to promote $ParB_F$-$ParB_F$ interactions *in vitro* (Taylor et al., 2021), further contributing to condensate disassembly.

Importantly, this disassembly is fully and rapidly reversible, as $ParB_F$ condensates reassemble within seconds following hexanediol removal, restoring initial fluorescence skewness levels (Fig. 5B). Such rapid re-assembly is consistent with the high dynamics observed in ParB complexes (Connolley et al., 2023; Osorio-Valeriano et al., 2021; Sanchez et al., 2015) and with the exchangeable nature of biomolecular condensates (Ladouceur et al., 2020). Alternatively, models based on sequential ParB loading at *parS*, followed by CTP-dependent clamp formation and sliding to mediate long-range DNA bridging (Connolley et

al., 2023; Osorio-Valeriano et al., 2021; Tisma et al., 2022), would require very high turnover rates. Such rate would be necessary to account for the rapid conversion of large numbers of ParB molecules into a condensed state and to sustain a nodal accumulation.

To date, only a single exception to the continuous presence of ParB condensates has been reported. In the predatory bacterium *Bdellovibrio bacteriovorus*, $ParB_{Bbac}$ condensates are absent during a defined developmental stage despite expression of $ParB_{Bba}$ (Kaljevic et al., 2023). The molecular basis of this stage-specific suppression of condensate formation remains unknown, but it correlates with the presence of short DNA segments adjacent to the two *parS* sites. This observation suggests that the initial binding step to $parS_{Bbac}$ may be inhibited by specific DNA context or structure, and possibly regulated through the action of a developmentally controlled factor to prevent ParB condensates assembly. Together, these observations support the view that while ParB condensates can assemble extremely rapidly once nucleation occurs at *parS*, modulation of this nucleation step may provide an efficient mechanism to regulate condensate formation in specific cellular contexts.

Mechanistic model of nucleation and stabilization

In nucleoid-containing cells, hexanediol treatment induced only partial disassembly of $ParB_F$ condensates, with fluorescence skewness plateauing at ~1.2 versus ~0.33 in nucleoid-free cells (Fig. 5B-C). This difference indicates that interactions with chromosomal DNA, most likely through non-specific binding, contribute to stabilizing ParB condensates and buffer them against complete dispersion. Such behavior is more consistent with a phase separation mechanism than with a model based solely on long-range ParB bridging interactions. In a purely bridging-based model (Connolley et al., 2023; Zhao et al., 2024), disruption of ParB-ParB interactions between clamps or the release of ParB clamps from *parS*-proximal DNA would be expected to yield comparable dispersion of ParB regardless of the presence of the chromosome. The pronounced difference observed between nucleoid-containing and nucleoid-depleted cells therefore argues for an additional stabilizing contribution arising from ParB-nsDNA interactions within the nucleoid environment. An alternative, non-exclusive possibility is that a subset of ParB clamps is loaded *in trans* onto chromosomal DNA, as reported *in vitro* for $ParB_{Bsub}$ (Tisma et al., 2022). In such a scenario, chromosome removal would release these ParB, allowing unrestricted diffusion, whereas in nucleoid-containing cells they would remain spatially constrained. However, this model would require a substantial fraction of $ParB_F$ to be loaded *in trans* relative to $parS_F$, a possibility that remains to be directly tested *in vivo*.

Consistent with a central role for ParB multimerization, the $ParB_F$-R156A variant, defective in $ParB_F$-$ParB_F$ interactions but still competent for clamp formation at $parS_F$ (Delimi et al., 2025), undergoes near-complete dissolution both in the presence or absence of chromosome (Fig. 5D, Fig. S5B-C). This result underscore the primary role of $ParB_F$ multimerization in condensate formation, while $ParB_F$-DNA interactions provide an additional stabilizing layer. Interestingly, the residual skewness observed in the presence of hexanediol (0.33) remains higher than that measured in cell lacking $parS_F$ (~0.19; Fig. 2C), suggesting that a fraction of $ParB_F$ dimers remains associated with $parS_F$ or persists as sliding clamps on $parS_F$-flanking DNA. These residual, potentially activated ParBs may serve as nucleation seeds, enabling rapid and efficient reassembly of condensates once hydrophobic interactions are restored.

Altogether, these observations support a model in which ParB condensates emerge from cooperative ParB-ParB and ParB-DNA interactions. ParB bound to $parS_F$ and subsequently converted into clamps on flanking DNA likely serves as a nucleation site for droplet formation. These clamped ParB species would function as activation seeds that recruit diffusive ParB, enabling the rapid and reversible condensate dynamics observed here. This mechanistic model aligns well with our recent proposal suggesting that clamped ParB species are activated intermediates promoting condensate formation (Delimi et al., 2025).

Conclusion

In summary, our findings further support the view that $ParB_F$ partition complexes are *bona fide* biomolecular condensates. They undergo rapid, reversible fusion and fission, display high mobility when untethered, and rely on multivalent interactions for assembly. We further show that $ParA_F$ acts not only as a spatial positioning factor but also as a key regulator of condensate coalescence. By preventing uncontrolled fusion of partition condensates while promoting their proper spatial distribution, $ParA_F$ ensures that multiple partition complexes remain as distinct entities within the same cell, thereby securing faithful DNA segregation.

More broadly, our results provide a biophysical framework for understanding bacterial DNA segregation as a process governed by regulated phase separation and ParA-type ATPase dynamics. Partition condensates exemplify how bacterial cells can exploit the physical principles of phase separation to achieve robust and controlled spatial organization. This work reinforces the growing concept that phase separation represents a conserved and versatile strategy for organizing membrane-less compartments across both prokaryotic and eukaryotic systems.

Experimental procedures

Bacterial strains, plasmids and oligonucleotides

All strains used in this study are derivatives of *E. coli* K12 and are listed, together with plasmids, in Table S1. Details of plasmid and strain construction are provided in the Supplemental experimental procedures. Briefly, strain LY643, which harbors four I-SceI sites (gift from C. Lesterlin), was modified to allow uniform induction of *para*$_{BAD}$*::I-sceI* by introducing the *Pcp18::araE* alleles (Bouet et al., 2006) via P1 transduction. To enhance chromosome DNA degradation efficiency, a *recA* mutation was also introduced, resulting in strain DLT4151.

All F and mini-F plasmids are derivatives of F1-10B (Debaugny et al., 2018) and pDAG114 (Bouet et al., 2006), respectively. F1-10B derivatives were introduced into recipient strains by conjugation, while pDAG114 derivatives were introduced by $CaCl_2$-transformation.

Epifluorescence microscopy

Strains expressing fluorescently tagged proteins were grown overnight at 30°C in M9 minimal medium supplemented with glucose and casamino acids (M9-glucose-CSA). Cultures were diluted 1:250 in fresh medium and incubated at 30°C until OD_{600nm} ~0.3. Cells were then either spotted (0.7 µl) onto M9-buffered 1% agarose pads or loaded into microfluidic devices (Chitozen slides, Idylle).

Fluorescence images were acquired as previously described (Diaz et al., 2015) using a Nikon epifluorescence microscope and NIS-Elements AR software (Nikon) for image capture and processing. Image analysis was performed using ImageJ softwares, with foci detection and positioning on the longitudinal cell axis carried out using the "*Coli inspector*" macro and the "*ObjectJ*" plugin, respectively.

For nucleoid staining, cells were incubated with DAPI (1 µg.ml^{-1}) for 10 min under shaking prior to loading into microfluidic slides, followed by continuous flow with M9-glucose medium containing DAPI (1 µg.ml^{-1}).

To quantify the ratio of ParB fluorescence intensity before and after fusion events, cells carrying two visible ParB condensates were selected. Regions of interest (ROIs) were manually drawn around each condensate in three consecutive frames before fusion, and the total fluorescence intensity was averaged. After fusion, a single ROI was drawn around the

merged condensate and the fluorescence was averaged over three consecutive frames. Background fluorescence from the medium was subtracted from all intensity measurements.

Skewness analyses

Individual cells were identified on phase-contrast images by cell segmentation using MicrobeJ. The resulting masks were subsequently applied to the corresponding fluorescence images for quantitative analysis. Skewness measurements, calculated using MicrobeJ plugin "*skewness*", measures the asymmetry of the pixel intensity distribution relative to the average fluorescence within each cell, providing a quantitative readout of condensate presence and compactness. Skewness values for each cell were automatically extracted and plotted using the BoxPlot function in the MicrobeJ plugin, based on the intensity.channel.skewness parameter.

Mean square displacement

Exponential growing cells, induced or not with 0.2% arabinose, were spotted onto 1% agarose pads buffered with M9-glucose medium. Time-lapse fluorescence microscopy was performed with images every 500 milliseconds over a 30-second period. ParB-mVenus foci were detected and tracked using the *TrackMate* plugin (Ershov et al., 2022) in Fiji. For each track, the position of the foci was recorded over time, and the MSD was calculated as a function of time lag. The diffusion coefficient (D) was estimated from the slope of the initial linear portion of the MSD curve, assuming Brownian diffusion. All fitting and statistical analyses were performed using custom scripts (See supplemental Material and methods for details).

Physical modeling

Details of the theoretical physics employed for physical modeling are described in Supplementary materials. It includes the description of polymer model and coarse-graining analyses, the calculation of the Critical surface tension (γ_{crit}) and of the free-energy equilibrium.

ACKNOWLEDGEMENTS

We are grateful to Julien Cayron and Christian Lesterlin for sharing the strain LY463 prior to publication. We are grateful to Jian Liu and Manuel Campos for critical reading of the manuscript and suggestions, and we thank Manuel Campos, Christian Lesterlin and Fabian

Erdel for insightful discussions. We also thank all members of the GeDy (CBI) and the SCPN (L2C) teams for fruitful discussions. This work was supported by the CNRS 80Prime MITI grant (ANCODS) and by the Agence National pour la Recherche (ANR-24-CE12-1319).

AUTHOR CONTRIBUTIONS

Conceptualization, J.-Y.B.;

Data curation, P.R., J.-Y.B.;

Formal analysis, L.D., J.C., J.-Y.B., and J.-C.W.;

Funding Acquisition, J.-Y.B.;

Investigation, P.R., L.D., J.C., J.R., J.-C.W., and J.-Y.B.;

Methodology, P.R., L.D., J.R., J.-C.W., and J.-Y.B.;

Project administration, J.-Y.B.;

Resources, F.C., J.-C.W., J.-Y.B.;

Supervision, J.-C.W., J.-Y.B.;

Validation, P.R., L.D., J.-C.W., and J.-Y.B.;

Visualization, P.R., J.-C.W. and J.-Y.B.;

Writing – Original draft, P.R., L.D., F.C., J.-C.W. and J.-Y.B.;

Writing – Review & Editing, P.R., L.D., F.C., J.-C.W., and J.-Y.B.

CONFLICT OF INTEREST STATEMENT

The authors declare that they have no conflicts of interest with the contents of this article.

ETHICS STATEMENT

This article does not contain any studies with human or animal subjects.

REFERENCES

Ah-Seng, Y., Rech, J., Lane, D., and Bouet, J.Y. (2013). Defining the role of ATP hydrolysis in mitotic segregation of bacterial plasmids. PLoS genetics *9*, e1003956.

Al-Husini, N., Tomares, D.T., Bitar, O., Childers, W.S., and Schrader, J.M. (2018). alpha-Proteobacterial RNA Degradosomes Assemble Liquid-Liquid Phase-Separated RNP Bodies. Mol Cell *71*, 1027-1039 e1014.

Alaoui, H.S., Quebre, V., Delimi, L., Rech, J., Debaugny-Diaz, R., Labourdette, D., Campos, M., Cornet, F., Walter, J.C., and Bouet, J.Y. (2025). In vivo assembly of bacterial

partition condensates on circular supercoiled and linear DNA. Mol Microbiol *123*, 232-244.

Alberti, S., Arosio, P., Best, R.B., Boeynaems, S., Cai, D., Collepardo-Guevara, R., Dignon, G.L., Dimova, R., Elbaum-Garfinkle, S., Fawzi, N.L., *et al.* (2025). Current practices in the study of biomolecular condensates: a community comment. Nature communications *16*, 7730.

Antar, H., Soh, Y.M., Zamuner, S., Bock, F.P., Anchimiuk, A., Rios, P.L., and Gruber, S. (2021). Relief of ParB autoinhibition by parS DNA catalysis and recycling of ParB by CTP hydrolysis promote bacterial centromere assembly. Science advances *7*, eabj2854.

Azaldegui, C.A., Swasthi, H.M., Hu, L., Pulianmackal, L.T., Rivett-Trznadel, H., Liu, J., Vecchiarelli, A.G., and Biteen, J.S. (2026). The kinetics and mobility of a ParA ATPase drive carboxysome distribution in Halothiobacillus neapolitanus. bioRxiv *10.64898*.

Azaldegui, C.A., Vecchiarelli, A.G., and Biteen, J.S. (2021). The emergence of phase separation as an organizing principle in bacteria. Biophys J *120*, 1123-1138.

Babl, L., Giacomelli, G., Ramm, B., Gelmroth, A.K., Bramkamp, M., and Schwille, P. (2022). CTP-controlled liquid-liquid phase separation of ParB. J Mol Biol *434*, 167401.

Bakshi, S., Siryaporn, A., Goulian, M., and Weisshaar, J.C. (2012). Superresolution imaging of ribosomes and RNA polymerase in live Escherichia coli cells. Mol Microbiol.

Balaguer, F.A., Aicart-Ramos, C., Fisher, G.L., de Braganca, S., Martin-Cuevas, E.M., Pastrana, C.L., Dillingham, M.S., and Moreno-Herrero, F. (2021). CTP promotes efficient ParB-dependent DNA condensation by facilitating one-dimensional diffusion from parS. eLife *10*.

Basalla, J.L., Mak, C.A., Byrne, J.A., Ghalmi, M., Hoang, Y., and Vecchiarelli, A.G. (2023). Dissecting the phase separation and oligomerization activities of the carboxysome positioning protein McdB. eLife *12*.

Boeynaems, S., Alberti, S., Fawzi, N.L., Mittag, T., Polymenidou, M., Rousseau, F., Schymkowitz, J., Shorter, J., Wolozin, B., Van Den Bosch, L., *et al.* (2018). Protein Phase Separation: A New Phase in Cell Biology. Trends Cell Biol *28*, 420-435.

Bouet, J.Y., Ah-Seng, Y., Benmeradi, N., and Lane, D. (2007). Polymerization of SopA partition ATPase: regulation by DNA binding and SopB. Mol Microbiol *63*, 468-481.

Bouet, J.Y., Bouvier, M., and Lane, D. (2006). Concerted action of plasmid maintenance functions: partition complexes create a requirement for dimer resolution. Mol Microbiol *62*, 1447-1459.

Bouet, J.Y., and Funnell, B.E. (2019). Plasmid Localization and Partition in Enterobacteriaceae. EcoSal Plus *8:10.1128/ecosalplus.ESP-0003-2019*.

Byczkowski, T., Małecki, J., and Ryznar, M. (2013). Hitting times of Bessel processes. Potential Analysis *38*, 753-786.

Byrne, J.A., Swasthi, H.M., Hu, L., Azaldegui, C.A., Liu, J., and Vecchiarelli, A.G. (2025). Tuning the interaction of a ParA-type ATPase with its partner separates bacterial organelle positioning from partitioning. bioRxiv *2025.05.22.655647*.

Castaing, J.P., Bouet, J.Y., and Lane, D. (2008). F plasmid partition depends on interaction of SopA with non-specific DNA. Mol Microbiol *70*, 1000-1011.

Cohan, M.C., and Pappu, R.V. (2020). Making the Case for Disordered Proteins and Biomolecular Condensates in Bacteria. Trends in biochemical sciences *45*, 668-680.

Connolley, L., Schnabel, L., Thanbichler, M., and Murray, S.M. (2023). Partition complex structure can arise from sliding and bridging of ParB dimers. Nature communications *14*, 4567.

Debaugny, R.E., Sanchez, A., Rech, J., Labourdette, D., Dorignac, J., Geniet, F., Palmeri, J., Parmeggiani, A., Boudsocq, F., Anton Leberre, V., *et al.* (2018). A conserved mechanism

drives partition complex assembly on bacterial chromosomes and plasmids. Mol Syst Biol *14*, e8516.
Delimi, L., Revoil, P., Bouet, J.-Y., and Walter, J.-C. (2025). The ParB-CTP cycle activates phase separation in bacterial DNA segregation Nucleic Acids Res *53*, gkaf944.
Diaz, R., Rech, J., and Bouet, J.Y. (2015). Imaging centromere-based incompatibilities: Insights into the mechanism of incompatibility mediated by low-copy number plasmids. Plasmid *80*, 54-62.
Donczew, M., Mackiewicz, P., Wrobel, A., Flardh, K., Zakrzewska-Czerwinska, J., and Jakimowicz, D. (2016). ParA and ParB coordinate chromosome segregation with cell elongation and division during Streptomyces sporulation. Open biology *6*.
Ershov, D., Phan, M.S., Pylvanainen, J.W., Rigaud, S.U., Le Blanc, L., Charles-Orszag, A., Conway, J.R.W., Laine, R.F., Roy, N.H., Bonazzi, D., *et al.* (2022). TrackMate 7: integrating state-of-the-art segmentation algorithms into tracking pipelines. Nat Methods *19*, 829-832.
Guilhas, B., Walter, J.C., Rech, J., David, G., Walliser, N.O., Palmeri, J., Mathieu-Demaziere, C., Parmeggiani, A., Bouet, J.Y., Le Gall, A., *et al.* (2020). ATP-Driven Separation of Liquid Phase Condensates in Bacteria. Mol Cell *79*, 293-303 e294.
Holland, J., Castrejon-Pita, A.A., Tuinier, R., Aarts, D., and Nott, T.J. (2023). Surface tension measurement and calculation of model biomolecular condensates. Soft matter *19*, 8706-8716.
Hu, L., Rech, J., Bouet, J.Y., and Liu, J. (2021). Spatial control over near-critical-point operation ensures fidelity of ParABS-mediated DNA partition. Biophys J *120*, 3911-3924.
Hu, L., Vecchiarelli, A.G., Mizuuchi, K., Neuman, K.C., and Liu, J. (2015). Directed and persistent movement arises from mechanochemistry of the ParA/ParB system. Proc Natl Acad Sci U S A *112*, E7055-7064.
Hwang, L.C., Vecchiarelli, A.G., Han, Y.W., Mizuuchi, M., Harada, Y., Funnell, B.E., and Mizuuchi, K. (2013). ParA-mediated plasmid partition driven by protein pattern self-organization. Embo J *32*, 1238-1249.
Hyman, A.A., Weber, C.A., and Julicher, F. (2014). Liquid-liquid phase separation in biology. Annual review of cell and developmental biology *30*, 39-58.
Jalal, A.S., Tran, N.T., and Le, T.B. (2020). ParB spreading on DNA requires cytidine triphosphate in vitro. eLife *9*, e53515.
Jalal, A.S., Tran, N.T., Stevenson, C.E., Chimthanawala, A., Badrinarayanan, A., Lawson, D.M., and Le, T.B. (2021). A CTP-dependent gating mechanism enables ParB spreading on DNA. eLife *10*.
Jalal, A.S.B., and Le, T.B.K. (2020). Bacterial chromosome segregation by the ParABS system. Open biology *10*, 200097.
Kaljevic, J., Tesseur, C., Le, T.B.K., and Laloux, G. (2023). Cell cycle-dependent organization of a bacterial centromere through multi-layered regulation of the ParABS system. PLoS genetics *19*, e1010951.
Kroschwald, S., Maharana, S, Simon, A. (2017). Hexanediol: a chemical probe to investigate the material properties of membrane-less compartments. Matters *3*, e201702000010.
Ladouceur, A.M., Parmar, B.S., Biedzinski, S., Wall, J., Tope, S.G., Cohn, D., Kim, A., Soubry, N., Reyes-Lamothe, R., and Weber, S.C. (2020). Clusters of bacterial RNA polymerase are biomolecular condensates that assemble through liquid-liquid phase separation. Proc Natl Acad Sci U S A *117*, 18540-18549.
Le Gall, A., Cattoni, D.I., Guilhas, B., Mathieu-Demaziere, C., Oudjedi, L., Fiche, J.B., Rech, J., Abrahamsson, S., Murray, H., Bouet, J.Y., *et al.* (2016). Bacterial partition complexes segregate within the volume of the nucleoid. Nature communications *7*, 12107.

Lee, P.S., and Grossman, A.D. (2006). The chromosome partitioning proteins Soj (ParA) and Spo0J (ParB) contribute to accurate chromosome partitioning, separation of replicated sister origins, and regulation of replication initiation in Bacillus subtilis. Mol Microbiol *60*, 853-869.

Lim, H.C., Surovtsev, I.V., Beltran, B.G., Huang, F., Bewersdorf, J., and Jacobs-Wagner, C. (2014). Evidence for a DNA-relay mechanism in ParABS-mediated chromosome segregation. eLife *3*, e02758.

Lin, D.C.H., and Grossman, A.D. (1998). Identification and characterization of a bacterial chromosome partitioning site. Cell *92*, 675-685.

Livny, J., Yamaichi, Y., and Waldor, M.K. (2007). Distribution of centromere-like parS sites in bacteria: insights from comparative genomics. J Bacteriol *189*, 8693-8703.

MacCready, J.S., Basalla, J.L., and Vecchiarelli, A.G. (2020). Origin and Evolution of Carboxysome Positioning Systems in Cyanobacteria. Mol Biol Evol.

MacCready, J.S., Hakim, P., Young, E.J., Hu, L., Liu, J., Osteryoung, K.W., Vecchiarelli, A.G., and Ducat, D.C. (2018). Protein gradients on the nucleoid position the carbon-fixing organelles of cyanobacteria. eLife *7*.

Monterroso, B., Margolin, W., Boersma, A.J., Rivas, G., Poolman, B., and Zorrilla, S. (2024). Macromolecular Crowding, Phase Separation, and Homeostasis in the Orchestration of Bacterial Cellular Functions. Chemical reviews *124*, 1899-1949.

Osorio-Valeriano, M., Altegoer, F., Das, C.K., Steinchen, W., Panis, G., Connolley, L., Giacomelli, G., Feddersen, H., Corrales-Guerrero, L., Giammarinaro, P.I., *et al.* (2021). The CTPase activity of ParB determines the size and dynamics of prokaryotic DNA partition complexes. Mol Cell *81*, 3992-4007 e3910.

Osorio-Valeriano, M., Altegoer, F., Steinchen, W., Urban, S., Liu, Y., Bange, G., and Thanbichler, M. (2019). ParB-type DNA Segregation Proteins Are CTP-Dependent Molecular Switches. Cell *179*, 1512-1524 e1515.

Parry, B.R., Surovtsev, I.V., Cabeen, M.T., O'Hern, C.S., Dufresne, E.R., and Jacobs-Wagner, C. (2014). The bacterial cytoplasm has glass-like properties and is fluidized by metabolic activity. Cell *156*, 183-194.

Pillet, F., Sanchez, A., Lane, D., Anton Leberre, V., and Bouet, J.Y. (2011). Centromere binding specificity in assembly of the F plasmid partition complex. Nucleic Acids Res *39*, 7477-7486.

Planchenault, C., Pons, M.C., Schiavon, C., Siguier, P., Rech, J., Guynet, C., Dauverd-Girault, J., Cury, J., Rocha, E.P.C., Junier, I., *et al.* (2020). Intracellular Positioning Systems Limit the Entropic Eviction of Secondary Replicons Toward the Nucleoid Edges in Bacterial Cells. J Mol Biol *432*, 745-761.

Puentes-Rodriguez, S.G., Norcross, J.D., and Mera, P.E. (2023). To let go or not to let go: how ParA can impact the release of the chromosomal anchoring in Caulobacter crescentus. Nucleic Acids Res *51*, 12275-12287.

Sanamrad, A., Persson, F., Lundius, E.G., Fange, D., Gynna, A.H., and Elf, J. (2014). Single-particle tracking reveals that free ribosomal subunits are not excluded from the Escherichia coli nucleoid. Proc Natl Acad Sci U S A *111*, 11413-11418.

Sanchez, A., Cattoni, D.I., Walter, J.C., Rech, J., Parmeggiani, A., Nollmann, M., and Bouet, J.Y. (2015). Stochastic Self-Assembly of ParB Proteins Builds the Bacterial DNA Segregation Apparatus. Cell Syst *1*, 163-173.

Shebelut, C.W., Guberman, J.M., van Teeffelen, S., Yakhnina, A.A., and Gitai, Z. (2010). Caulobacter chromosome segregation is an ordered multistep process. Proc Natl Acad Sci U S A.

Shin, Y., and Brangwynne, C.P. (2017). Liquid phase condensation in cell physiology and disease. Science *357*.

Soh, Y.M., Davidson, I.F., Zamuner, S., Basquin, J., Bock, F.P., Taschner, M., Veening, J.W., De Los Rios, P., Peters, J.M., and Gruber, S. (2019). Self-organization of parS centromeres by the ParB CTP hydrolase. Science *366*, 1129-1133.

Stracy, M., Schweizer, J., Sherratt, D.J., Kapanidis, A.N., Uphoff, S., and Lesterlin, C. (2021). Transient non-specific DNA binding dominates the target search of bacterial DNA-binding proteins. Mol Cell *81*, 1499-1514.

Taylor, J.A., Seol, Y., Budhathoki, J., Neuman, K.C., and Mizuuchi, K. (2021). CTP and parS coordinate ParB partition complex dynamics and ParA-ATPase activation for ParABS-mediated DNA partitioning. eLife *10*.

Tisma, M., Janissen, R., Antar, H., Martin-Gonzalez, A., Barth, R., Beekman, T., van der Torre, J., Michieletto, D., Gruber, S., and Dekker, C. (2023). Dynamic ParB-DNA interactions initiate and maintain a partition condensate for bacterial chromosome segregation. Nucleic Acids Res *51*, 11856-11875.

Tisma, M., Kaljevic, J., Gruber, S., Le, T.B.K., and Dekker, C. (2024). Connecting the dots: key insights on ParB for chromosome segregation from single-molecule studies. FEMS microbiology reviews *48*.

Tisma, M., Panoukidou, M., Antar, H., Soh, Y.M., Barth, R., Pradhan, B., Barth, A., van der Torre, J., Michieletto, D., Gruber, S., *et al.* (2022). ParB proteins can bypass DNA-bound roadblocks via dimer-dimer recruitment. Science advances *8*, eabn3299.

Vecchiarelli, A.G., Han, Y.W., Tan, X., Mizuuchi, M., Ghirlando, R., Biertumpfel, C., Funnell, B.E., and Mizuuchi, K. (2010). ATP control of dynamic P1 ParA-DNA interactions: a key role for the nucleoid in plasmid partition. Mol Microbiol *78*, 78-91.

Walter, J.C., Dorignac, J., Lorman, V., Rech, J., Bouet, J.Y., Nollmann, M., Palmeri, J., Parmeggiani, A., and Geniet, F. (2017). Surfing on Protein Waves: Proteophoresis as a Mechanism for Bacterial Genome Partitioning. Phys Rev Lett *119*, 028101.

Walter, J.C., Rech, J., Walliser, N.O., Dorignac, J., Geniet, F., Palmeri, J., Parmeggiani, A., and Bouet, J.Y. (2020). Physical Modeling of a Sliding Clamp Mechanism for the Spreading of ParB at Short Genomic Distance from Bacterial Centromere Sites. iScience *23*, 101861.

Zhao, Y., Guo, L., Hu, J., Ren, Z., Li, Y., Hu, M., Zhang, X., Bi, L., Li, D., Ma, H., *et al.* (2024). Phase-separated ParB enforces diverse DNA compaction modes and stabilizes the parS-centered partition complex. Nucleic Acids Res.

FIGURES LEGEND

Figure 1: ParB partition condensates coalescence in the absence of nucleoid.

A- Schematic representation of the inducible chromosome degradation system. I-Sce1 endonuclease cuts at the four specific sites. RecBCD complexes specifically degrade the chromosome but not plasmid DNA from the double strands breaks (black arrows).

B- Fluorescence microcopy of chromosome degradation and fusion events. Series of images of the same cell, stained with DAPI, at 40, 80 and 120 min post-arabinose induction, observed in the blue (left panels) and yellow (right panels) channels, to monitor chromosome degradation and ParB-mVenus condensates. Scale bar, 1 µm.

C- Distribution of the number of ParB-mVenus foci. The number of foci per cell before (T0; black) and after (T120; grey) chromosome degradation is displayed for the plasmid F (F1-10B04; left), the miniF (pJYB234; middle) and the miniF Δ*parAB* (pPER07; right).

D- Distribution of ParB-mVenus fusion events over time. Images (as in B) were acquired every two minutes between 40 and 120 min after arabinose induction. The number of cells displaying a fusion event were shown per time intervals. The solid line represents the cumulative fraction of chromosome-less cells displaying a fusion event. The dotted line represents the degradation of the chromosome over time (from Fig. S1B). N corresponds to the number of cell analyzed.

Figure 2: Coalescence depends on properly assembled ParB condensates

A- Time-lapse imaging of $ParB_F$-R156A-mVenus. (top) Series of images acquired at 0, 40, 80 and 120 minutes post-arabinose induction (plasmid F1-10B15). Scale bar, 1 µm. (bottom) Distribution of the number of ParB-R156A-mVenus foci before (T0; black) and after (T120; grey) chromosome degradation.

B- Time-lapse imaging of $ParB_F$-mVenus from the F Δ*parA* plasmid. As in (A), with the plasmid F1-10B12.

C- Quantification of the ParB condensates assembly defect. Fluorescent images of $ParB_F$-mVenus or $ParB_F$-R156A-mVenus, from WT (N=144), Δ*parA* (N=152), Δ*parS* (N=411) or *parB*-R156A (N=269) plasmids in exponentially growing cells (no chromosome degradation) were subjected to Skewness analyses. Skewness analyses were displayed as box plots indicating the medians, the quartiles and the standard deviations, and average values are indicated on top of each box plot.

Figure 3: Coalescence into a single condensate is conservative.

A- Most ParB molecules regroups in the fused condensates. The box plot displays the ratio of the average ParB fluorescence intensity, measured on three successive images, after fusion events over the average sum of ParB-mVenus fluorescence intensity from two foci, measured on three successive images, before fusion events. The box plots indicates the median, quartiles and the standard deviation, with each dot representing a fusion event (N=50).

B- Numerous ParB condensates coalesce into a single one after chromosome degradation. (top) Imaging of $ParB_F$-mVenus from strain DLT 4161 (pJYB234), grown in the presence of cephalexin, after 40 and 120 min post-arabinose induction. The scale bar represents 1 µm. (bottom) Distribution of the number of ParB-mVenus foci before and after chromosome degradation. The number of foci per cell before (T0; black) and after (T120; grey) chromosome degradation is displayed for the plasmid mF pJYB234.

Figure 4: Coalescence of partition condensates is nearly instantaneous.

A- Transient splitting of ParB condensates in chromosome-depleted cells. Time-lapse fluorescence microscopy was performed after complete chromosome degradation (time > T120), with images acquired every 250 msec. Time is indicated in msec. Transient splitting and re-fusion of ParB-mVenus foci were frequently observed.

B- Splitting events are frequent. The frequency of splitting events was quantified in chromosome-depleted cells expressing ParB-mVenus from plasmid F or mini-F (mF), in the presence or absence of *parA* (Δ*parA*). N= 807 (F), 283 (mF), 120 (FΔ*parA*) and 86 (mFΔ*parA*).

C- Fusion occurs rapidly following splitting. A total of 111 chromosome-depleted cells carrying plasmid F and exhibiting a splitting event (as in A) were analyzed. The time elapsed between splitting and fusion was measured, revealing that fusion typically occurred within ~1 second. (*inset*) same data plotted in Log-Log scale (blue dots). The dotted red line corresponds to a power law with an exponent -3/2.

D- Partition condensates are highly mobile in the absence of the chromosome. Representative intracellular trajectories of ParB-mVenus foci tracked over time in cells carrying plasmid F or mini-F, either with (+chr) or without (no chr) the chromosome. Trajectories illustrate an important increase in mobility under chromosome-depleted conditions.

Figure 5: Assembly and disassembly of partition condensates occurs within seconds

A- Hexanediol disrupts ParB condensates but not DNA-bound proteins. Chromosome-depleted cells carrying the mini-F pJYB234 were imaged before (-Hex; left panels) and after (+Hex; right panels) a 1-minute incubation with 10% 1,6-hexanediol in the blue (top panels) or yellow channels (bottom panels) to visualize $ParB_F$-mTq2 or MalI-mNG[2], respectively.

B- Rapid and reversible disassembly of ParB condensates in nucleoid-free cells. (Left) Time-lapse imaging of chromosome-depleted cells expressing $ParB_F$-mVenus from plasmid F was performed using a microfluidic setup, allowing controlled infusion of hexanediol at time 0 (T0) and wash out at 100 sec (T100). (Right) Quantification of $ParB_F$-mVenus fluorescence skewness across > 1700 cells at each indicated time point. The rapid decrease in skewness upon Hex treatment and the fast recovery upon washout indicates a nearly instantaneous disassembly and reassembly of ParB condensates.

C- Rapid, reversible but partial disassembly of ParB condensates in cells with an intact chromosome. Same as in (B) but performed in cells with a nucleoid. Hex was washed out after 160 s of infusion. Fluorescence skewness was calculated from > 760 cells per time point.

D- Multiple interactions are involved in ParB condensate assembly. Fluorescence skewness was measured in cells expressing either $ParB_F$ (WT) or the interaction-defective variant $ParB_F$-R156A, from plasmid F, imaged before (T0) or after (T120) chromosome degradation, and either untreated (–Hex) or treated (+Hex) with hexanediol. Time-lapse microscopy was performed as in (B–C). The skewness levels in f, g and h are 0.33, 0.27 and 0.21, respectively.

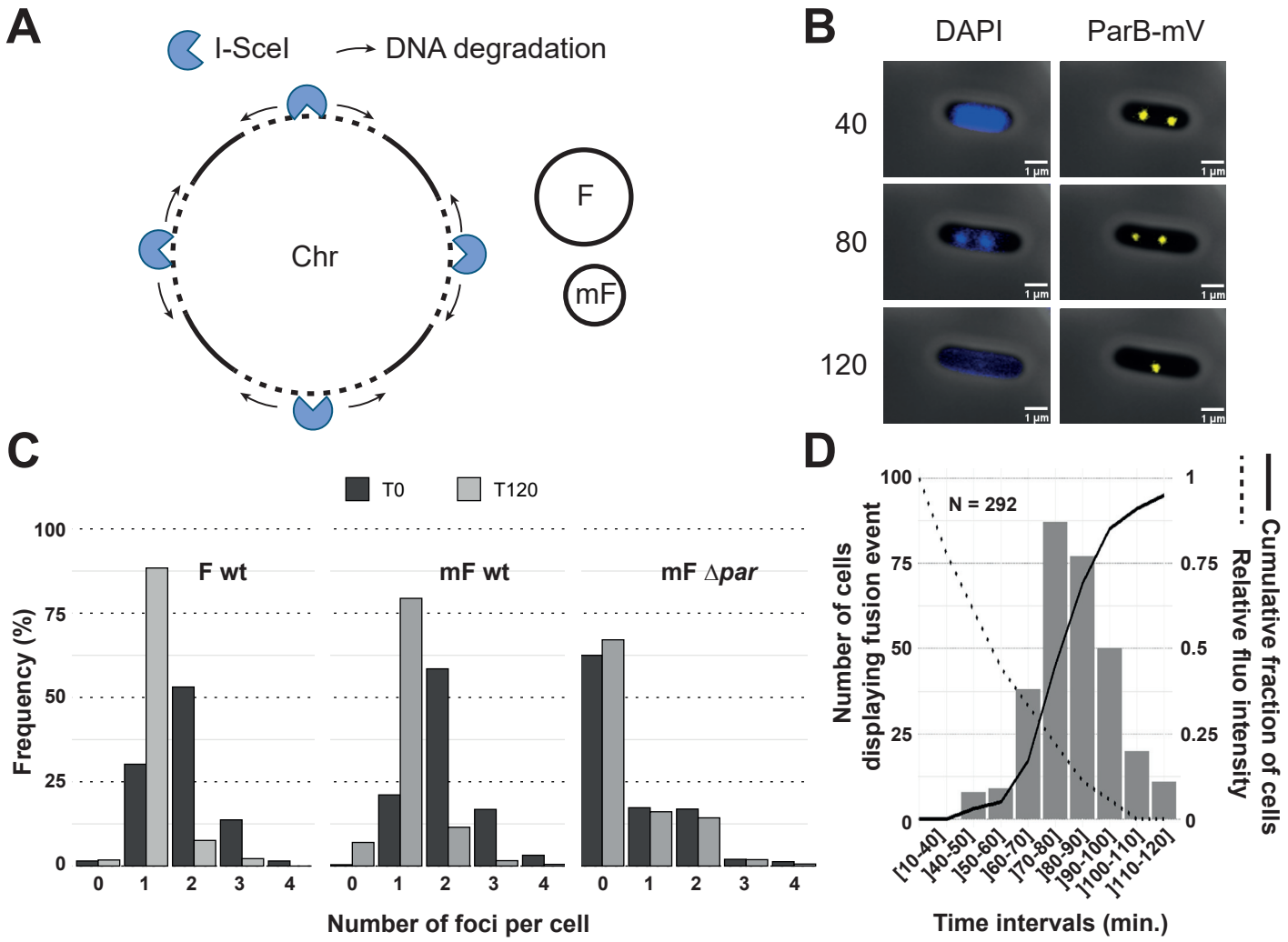
A
I-SceI
DNA degradation
Chr
F
mF
B
DAPI
ParB-mV
40
80
120
1 µm
C
T0
T120
F wt
mF wt
mF Δpar
Frequency (%)
Number of foci per cell
D
N = 292
Number of cells displaying fusion event
Cumulative fraction of cells
Relative fluo intensity
Time intervals (min.)
[10-40]
]40-50]
]50-60]
]60-70]
]70-80]
]80-90]
]90-100]
]100-110]
]110-120]

Figure 1

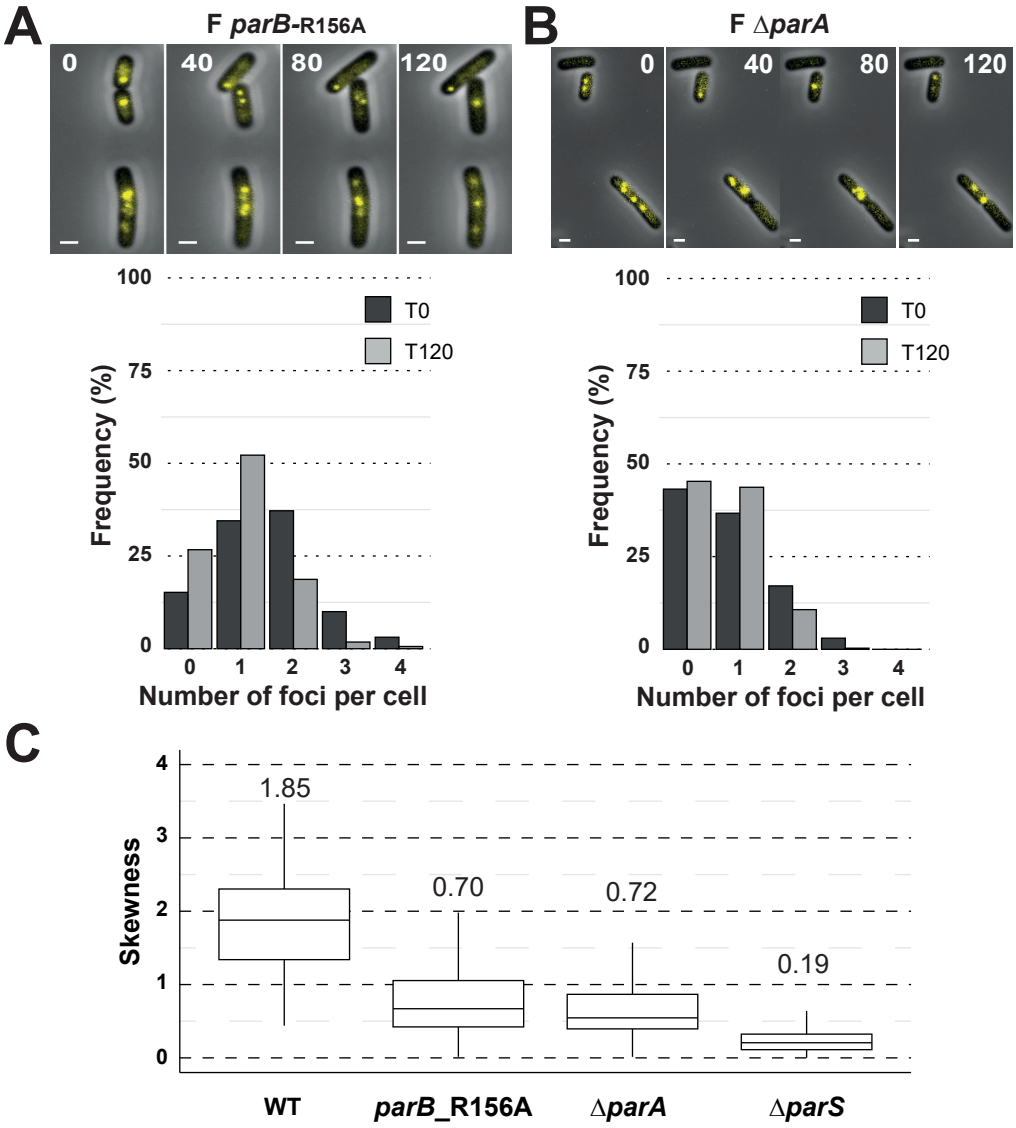
A
F parB-R156A
0
40
80
120
B
F ΔparA
0
40
80
120
100
75
50
25
0
Frequency (%)
T0
T120
0
1
2
3
4
Number of foci per cell
C
4
3
2
1
0
Skewness
1.85
0.70
0.72
0.19
WT
parB_R156A
ΔparA
ΔparS

Figure 2

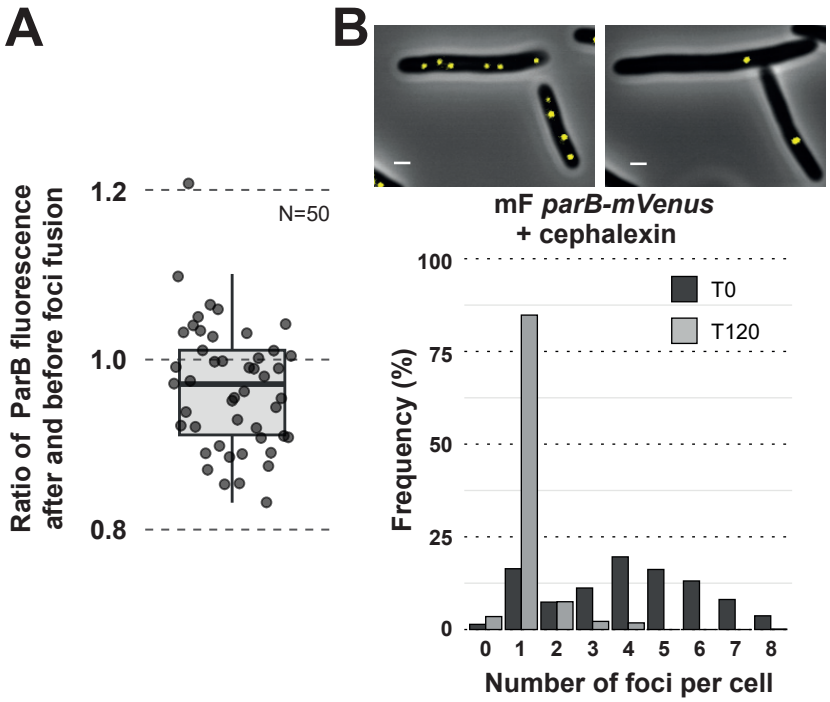
A
B
Ratio of ParB fluorescence after and before foci fusion
1.2
1.0
0.8
N=50
mF parB-mVenus
+ cephalexin
T0
T120
Frequency (%)
100
75
50
25
0
0 1 2 3 4 5 6 7 8
Number of foci per cell

Figure 3

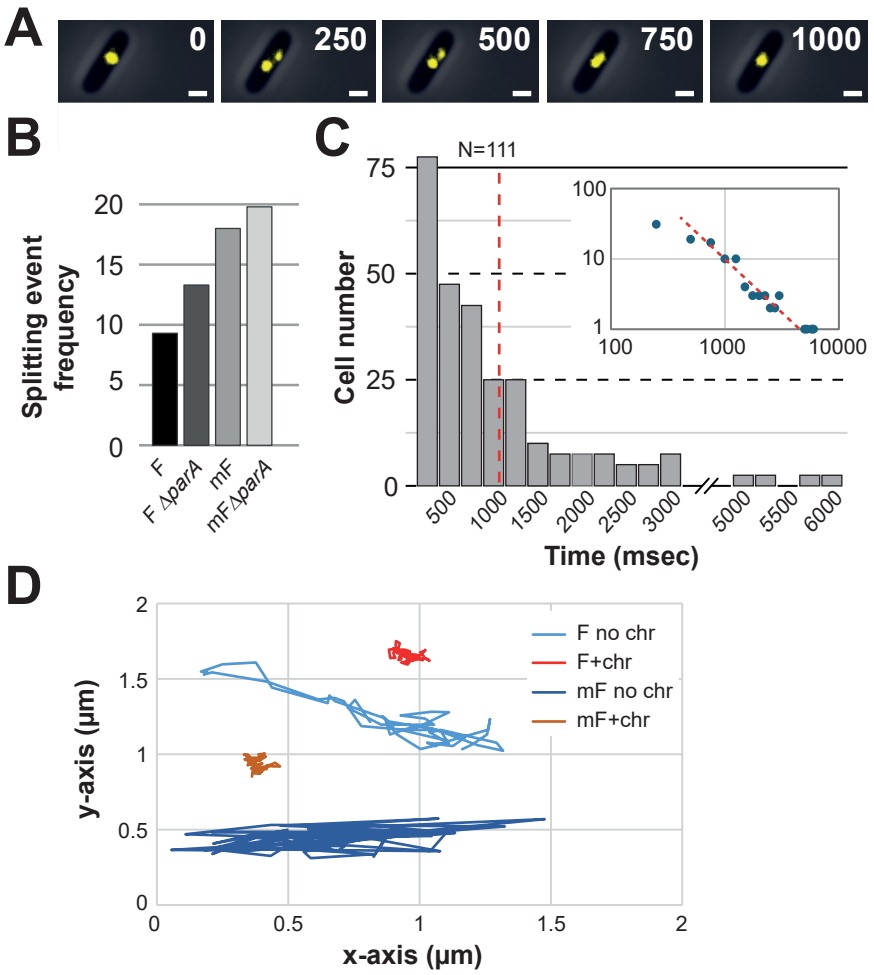
A
0
250
500
750
1000
B
Splitting event frequency
20
15
10
5
0
F
F ΔparA
mF
mF ΔparA
C
N=111
Cell number
75
50
25
0
100
10
1
100
1000
10000
500
1000
1500
2000
2500
3000
5000
5500
6000
Time (msec)
D
y-axis (µm)
2
1.5
1
0.5
0
0
0.5
1
1.5
2
x-axis (µm)
F no chr
F+chr
mF no chr
mF+chr

Figure 4

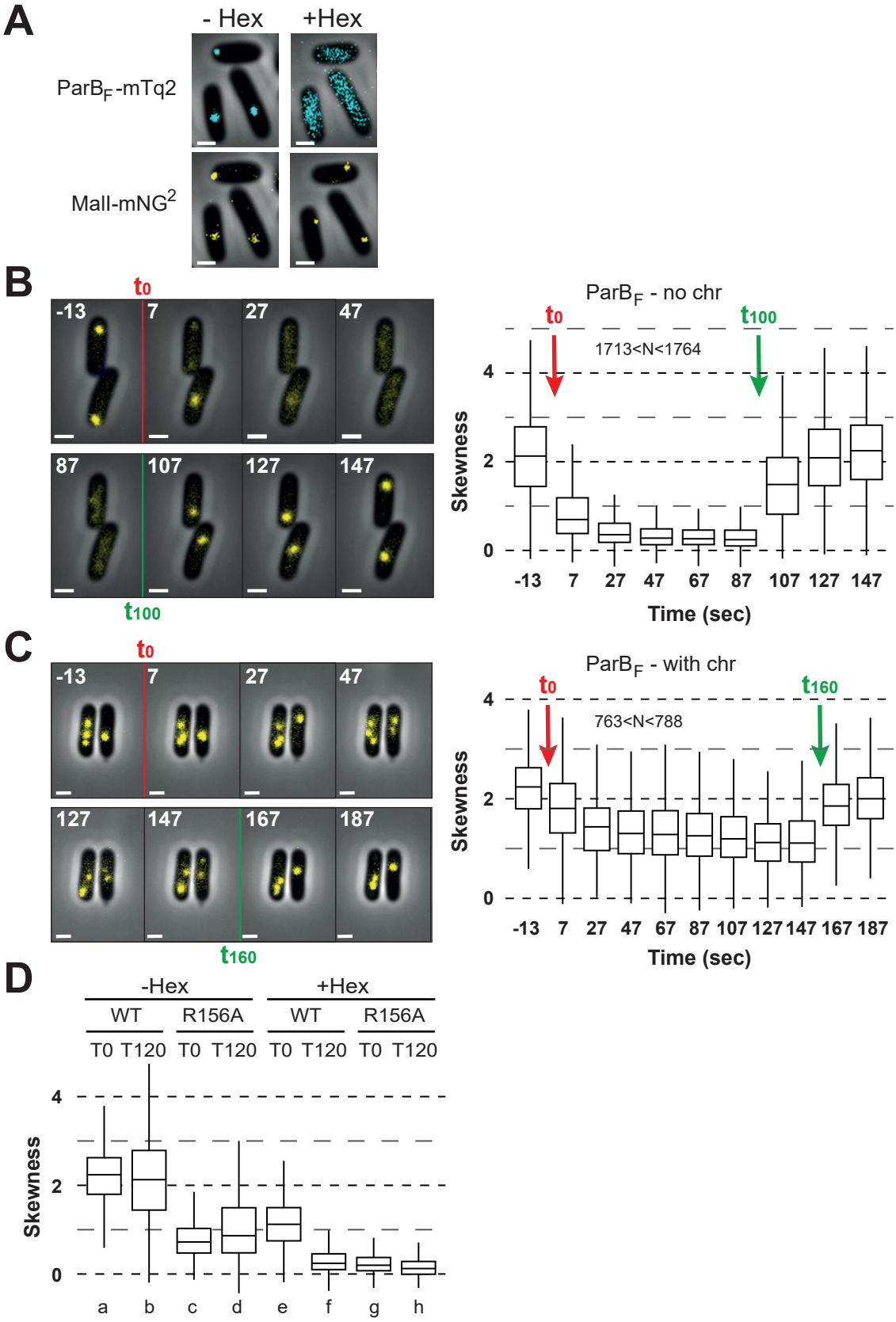
A
- Hex
+Hex
ParB$_F$-mTq2
MalI-mNG^2
B
t_0
-13
7
27
47
87
107
127
147
t_{100}
ParB$_F$ - no chr
1713<N<1764
Skewness
Time (sec)
C
t_0
127
147
167
187
t_{160}
ParB$_F$ - with chr
763<N<788
D
-Hex
+Hex
WT
R156A
T0 T120
a b c d e f g h

Figure 5